

## Multi-instrument analysis of electron populations in Saturn's magnetosphere

P. Schippers,<sup>1</sup> M. Blanc,<sup>1</sup> N. André,<sup>2</sup> I. Dandouras,<sup>1</sup> G. R. Lewis,<sup>3</sup> L. K. Gilbert,<sup>3</sup> A. M. Persoon,<sup>4</sup> N. Krupp,<sup>5</sup> D. A. Gurnett,<sup>4</sup> A. J. Coates,<sup>3</sup> S. M. Krimigis,<sup>6</sup> D. T. Young,<sup>7</sup> and M. K. Dougherty<sup>8</sup>

Received 15 February 2008; revised 2 May 2008; accepted 7 May 2008; published 18 July 2008.

[1] We analyze the radial distribution of electron populations inside  $20 R_s$  in Saturn's magnetosphere, and we calculate moments for these populations by a forward modeling method using composite spectra produced by the CAPS/ELS (0.6 eV to 26 keV) and the MIMI/LEMMS (15 keV to 10 MeV) instruments on board Cassini. We first calculate and harmonize both data sets in physical units and apply corrections taking into account biases introduced by spacecraft interaction with the magnetospheric environment. We then test different bimodal isotropic electron distribution models, deciding on a model with two kappa distributions. We adjust our isotropic model to the flux composite spectra with a least square method to produce three sets of fluid parameters (density, temperature, spectral index) per electron population. The radial profiles are then analyzed, revealing a relevant boundary at  $9 R_s$  in both thermal and suprathermal electron populations. Observed discontinuities in the moment profiles (sudden drop-off in cold density profile outside  $9 R_s$ , hot electrons drop-off inside  $9 R_s$ ) coincide with the known outer edge of Saturn's neutral OH cloud. Farther out, thermal electrons disappear completely beyond  $15 R_s$  while suprathermal electrons are still observed in the middle and outer magnetosphere.

**Citation:** Schippers, P., et al. (2008), Multi-instrument analysis of electron populations in Saturn's magnetosphere, *J. Geophys. Res.*, 113, A07208, doi:10.1029/2008JA013098.

### 1. Introduction

[2] Saturn's plasma environment was first sampled by Pioneer 11 [Frank *et al.*, 1980] and later detailed by the three charged particle instruments on board the two Voyager spacecraft: the Plasma Science (PLS) [Bridge *et al.*, 1981, 1982] and the Low Energy Charged Particle (LECP) [Krimigis *et al.*, 1981, 1983] experiments, and the Cosmic Ray System (CRS) [Vogt *et al.*, 1981, 1982]. These flybys revealed a unique and complex magnetosphere, host of various distributed internal and external plasma sources (the planetary ionosphere, the ring system, Saturn's numer-

ous icy satellites, Titan as well as the solar wind and cosmic rays particles), where electrons play an important role as tracers of the chemical, physical, and transport processes that operate in the environment [Randall, 1994].

[3] A comprehensive analysis of Voyager electron observations, merging the information from the three instruments, has been performed by Maurice *et al.* [1996]. They carefully intercalibrated all available data to produce composite electron energy spectra over a broad range of energies, from 10 eV to 2 MeV and ultimately computed three moments (density, pressure, and electron current density) of the electron distribution function, assumed to have isotropic angular distribution, along the two Voyager trajectories.

[4] Since July 2004, Cassini has been in orbit around Saturn providing new measurements of the electrons in Saturn's magnetosphere. Two instruments on board Cassini measure these populations, the Electron Spectrometer of the Cassini Plasma Spectrometer (CAPS/ELS) [Young *et al.*, 2004] and the Low Energy Magnetospheric Measurements System of the Magnetospheric Imaging Instrument (MIMI/LEMMS) [Krimigis *et al.*, 2004]. Thanks to some overlap of their energy range, these instruments provide a continuous coverage of electron populations from a few eV to a few tens of MeV. Our long-term objective is to study the radial, latitudinal, and local time dependence of the different electron populations using all Cassini orbits and to provide a comprehensive empirical model of the electron popula-

<sup>1</sup>Centre d'Etude Spatiale des Rayonnements, CNRS/Université Paul Sabatier, Toulouse, France.

<sup>2</sup>Research and Scientific Support Department, European Space Agency, Noordwijk, Netherlands.

<sup>3</sup>Mullard Space Science Laboratory, University College London, Dorking, UK.

<sup>4</sup>Department of Physics and Astronomy, University of Iowa, Iowa City, Iowa, USA.

<sup>5</sup>Max-Planck-Institut für Sonnensystemforschung, Katlenburg-Lindau, Germany.

<sup>6</sup>Johns Hopkins University Applied Physics Laboratory, Laurel, Maryland, USA.

<sup>7</sup>Southwest Research Institute, San Antonio, Texas, USA.

<sup>8</sup>Department of Space and Atmospheric Physics, Imperial College London, London, UK.

tions within Saturn's magnetosphere. In this study, we present a first unifying analysis of the electron populations by merging the new Cassini data sets into one single consistent description.

[5] In section 2, we detail the instruments and the data used to extract electron intensity composite spectra. We discuss the method applied in order to obtain electron moments over a broad energy range. In section 3, we analyze the radial distribution of electron populations for one particular Cassini orbit and identify relevant plasma boundaries and processes. In section 4, we discuss our results and conclude our study.

## 2. Instrumentation, Data Sets, and Derivation of Electron Moments

[6] The CAPS/ELS instrument is an electrostatic analyzer that measures electron count rates from 0.56 eV to 26 keV in 63 logarithmically spaced energy channels. The eight anodes of the instrument are mounted on a turntable partially rotating around the  $z$ -axis of the spacecraft, which allows a spatial coverage of  $160^\circ$  in elevation and  $208^\circ$  in azimuth.

[7] The MIMI/LEMMS instrument is a two-ended telescope that utilizes solid state detectors to measure electron energy and count rates from 15 keV to 884 keV in its low-energy end (energy channels C0–C7), and from 0.1 to about 10 MeV in its high-energy end (energy channels E0–E7). The instrument is mounted on a rotating platform, which allows a good pitch angle coverage by turning around the  $-y$ -axis of the spacecraft typically every 86 s. However, the position of the instrument had to be locked in safe position after 4.5 orbits around Saturn due to a technical problem, which strongly limits the pitch angle coverage for the following orbits.

[8] These two instruments use different technologies, with different fields of view. In order to obtain composite electron spectra from these instruments, we first harmonize both data sets in common physical units, independently of the geometry of the instruments. As common units, we use differential number flux (DNF) or intensity, expressed in  $\text{keV}^{-1} \text{s}^{-1} \text{sr}^{-1} \text{cm}^{-2}$ . The DNF is calculated from the raw count rate ( $R_c$ ) using the currently available effective geometric factors for each instrument, calibrated on the ground.

[9] In the case of the CAPS/ELS electrostatic analyzer, the DNF is given by

$$\text{DNF} = \frac{R_c}{gE} \quad (1)$$

where  $g$  is the energy-independent geometric factor (in  $\text{cm}^2 \text{sr keV/keV}$ ) including energy resolution  $\Delta E/E$  (0.17) where  $E$  is the centroid energy value (in keV) of the channel. In the case of the MIMI/LEMMS solid state detector, the DNF is given by

$$\text{DNF} = \frac{R_c}{G\Delta E} \quad (2)$$

where  $G$  is the geometric factor (in  $\text{cm}^2 \text{sr}$ ) and  $\Delta E$  the energy bandwidth of the channel.

[10] In addition several effects need to be carefully analyzed and corrected, when possible, before our analysis can be done. First, the interaction of the spacecraft with the magnetospheric environment introduces several biases in the data. Penetrating high-energy particles contaminating the measurements are removed, particularly in the innermost regions of Saturn's magnetosphere. Spacecraft charging (positive or negative) also affects the measurements of the energy distribution of the particles. The spacecraft potential is determined using CAPS/ELS photoelectron observations [Lewis *et al.*, 2008] in order to correct our measurements (especially at low energies). Unfortunately, when the spacecraft potential is negative, like in the inner regions of Saturn's magnetosphere, it cannot be determined from the CAPS/ELS observations. In this case, we have to keep in mind that we do not have access to a part of the electron distribution. Reflected sunlight from parts of the spacecraft has to be removed from our measurements. The field of views of the instruments can also be obscured by parts of the spacecraft itself (e.g., RTG, thrusters, high-gain antenna). This obscuration has to be taken into account.

[11] A three-dimensional view of the resulting composite electron spectra is shown in Figure 1, in the case of the 24th orbit of Cassini (Rev. 24) which took place in the equatorial plane of the magnetosphere, with periapsis at  $5.4 R_s$ . It displays DNF as function of energy ( $y$ -axis, in keV) and radial distance to Saturn ( $x$ -axis, in Saturn radii,  $1 R_s = 60,268 \text{ km}$ ). Negative (positive) distances represent the inbound (outbound) leg of the Cassini trajectory. We restrict our analysis inside  $20 R_s$ , since most of the known plasma sources in the system orbit within this region. The observed gap between the highest ELS energy channel (26 keV) and the lowest MIMI/LEMMS energy channel (15–40 keV) appears to be due to a low signal to noise ratio of the high-energy channels of CAPS/ELS. We will illustrate in the next section our solution to correct this apparent discrepancy.

[12] A qualitative analysis of Figure 1 reveals what appears to be three different electron populations, corresponding to visible energy peaks in the composite spectra. In the innermost magnetosphere ( $\leq 7 R_s$ ), trapped electron radiation belts are observed at very high energy (2 MeV) and their intensity is observed to decrease rapidly when radial distance increases. A population of electrons at intermediate energy (100 eV–10 keV) is observed in most of the magnetosphere, with a maximum in intensity around  $10 R_s$  (clearly visible during the outbound leg for example). A population of cold electrons (below 100 eV) is also observed in most of the magnetosphere, with a maximum in intensity at closest approach ( $5.4 R_s$ ). These electron populations at low- and intermediate energy correspond to thermal and suprathermal electrons, respectively. The coexistence of these two populations in Saturn's magnetosphere was revealed by Sittler *et al.* [1983] using Voyager PLS observations and confirmed by Young *et al.* [2005] using CAPS observations. Their origin was addressed by Rymer *et al.* [2007], who have analyzed the variations with radial distance of their phase space densities. From their analysis, the thermal electrons are likely to have distributed sources in the inner magnetosphere, whereas the suprathermal electrons are likely to originate from Saturn's middle magnetosphere. We will now show that the electron population of very high

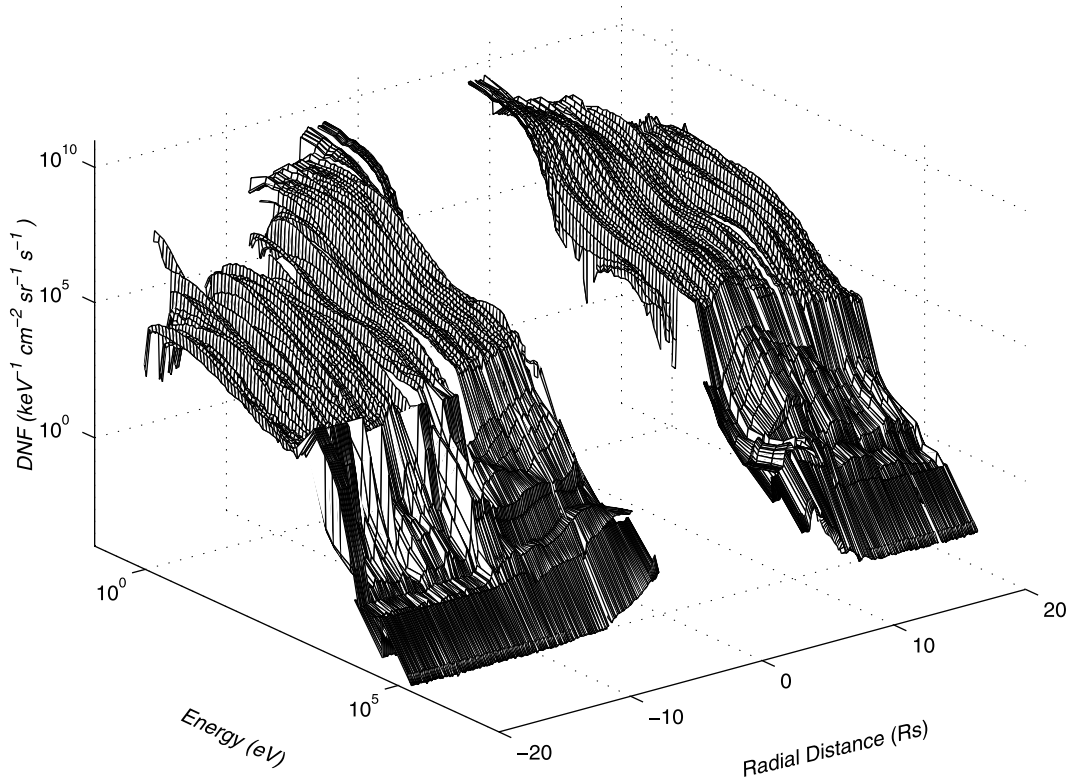


**Figure 1.** Three-dimensional plot of composite CAPS/ELS and MIMI/LEMMS electron intensities versus energy and radial distance, for Rev. 24 (days 140 to 144 of 2006).

energy corresponds in fact to the high-energy tail of the suprathermal electrons, extending into the MeV range.

[13] From our composite electron spectra, we use a forward modeling method to test different bimodal distribution functions to adjust with a least squares method our electron observations. We assume the electron populations to be isotropic. To solve the apparent discrepancy between the measurements of CAPS/ELS and MIMI/LEMMS, we do not consider the measurements obtained by the highest energy channels (above 15 keV) of CAPS/ELS, nor the not well constrained E0-E7 MIMI/LEMMS energy channels.

[14] In a first attempt, we model our two electron populations (thermal and suprathermal) by using Maxwellian distributions (four free parameters, illustrations given in Figure 2a). This model predicts fluxes that are too low and is not able to reproduce the tail of the distribution of the suprathermal population. In a second attempt, we model the thermal population using a Maxwellian distribution and the suprathermal population using a kappa distribution (five free parameters, illustrations given in Figure 2b). At low radial distances, this model appears to fit the data very well, for the two populations. However, farther out, the peak of the thermal population appears to broaden and this model does not appear accurate enough. In a third attempt, we use kappa distributions to model both populations (six free parameters, illustrations given in Figure 2c). This model appears very satisfactory, being now able to both reproduce the broadening of the peak of the thermal population and the high-energy tail of the suprathermal population extending into the MeV energy range.

[15] The main conclusion of our tests is that neither the thermal nor the suprathermal populations have Maxwellian shapes, which indicates that both populations are out-of-equilibrium. Having determined which model to use, we are now in a position to derive a set of electron fluid parameters (density  $n$ , temperature  $T$ , kappa index  $\kappa$ ) per electron population (denoted by adding the subscript cold (hot) for the thermal (suprathermal) population). In the next section, we analyze the radial distribution of these parameters for Rev. 24.

### 3. Radial Profiles of Electron Moments and Identification of Plasma Boundaries

[16] The fluid parameters of thermal (in blue) and suprathermal (in red) electron populations obtained from the combined CAPS/ELS and MIMI/LEMMS observations are shown in Figure 3, together with the corresponding CAPS/ELS energy-time spectrogram. From these radial profiles, we can identify two radial plasma boundaries where the properties of our electron populations change significantly. These two boundaries are observed at  $9 R_s$  and around  $13\text{--}15 R_s$ , both inbound and outbound. They delineate three different regions: Region 1, inside  $9 R_s$ ; Region 2, between  $9$  and  $13 R_s$ ; and Region 3, beyond  $13 R_s$ . The identification of these boundaries led us to consider each of these regions separately. In regions 1 and 2, we fit the observed profiles of densities, temperatures and kappa values with the help of power laws ( $aL^b + c$ ), for each electron population and without assuming any local time dependence of profiles. Table 1 summarizes the various

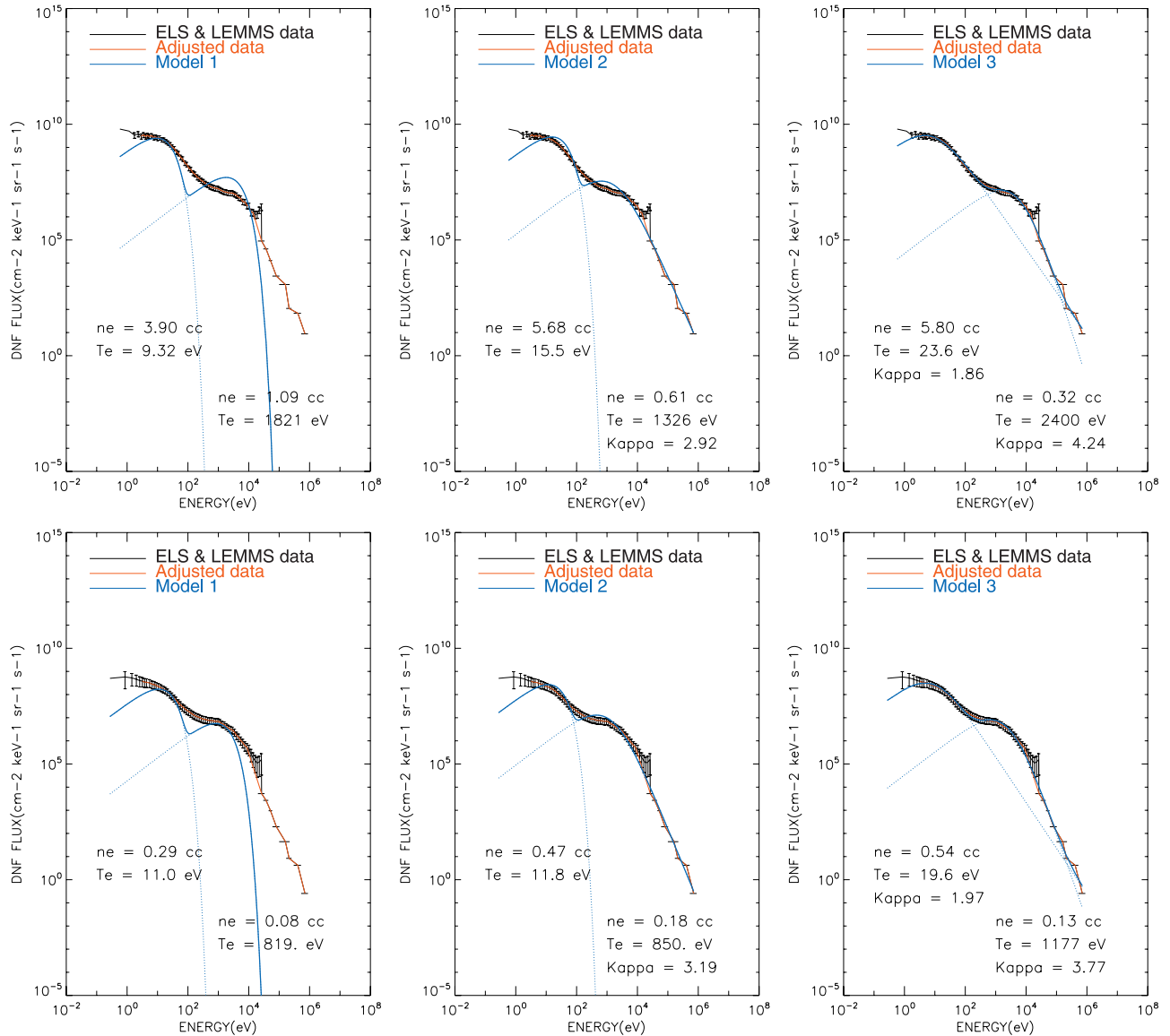


**Figure 2.** Composite CAPS/ELS and MIMI/LEMMS (energy channels C0-C7) spectral plots of electron intensities versus energy, observed at (top) 2200 UT ( $R = 9 R_s$ , local time 18.32 h, latitude 0.23 degrees) and at (bottom) 0727 UT ( $R = 12.8 R_s$ , local time 19.82 h, latitude 0.35 degrees) on days of year 142 and 143 of 2006 during Rev. 24, respectively. Original data are represented in black, our interpolated data are represented in red, and the results of our various models are represented in blue. (left) Model with 2 Maxwellian distributions. (middle) Model with one Maxwellian and one kappa distribution. (right) Model with two kappa distributions.

obtained values for parameters  $a$ ,  $b$ , and  $c$ . We compared our density and thermal electron temperature values calculated by the forward modeling method detailed in this paper, with the thermal moments profiles from *Sittler et al.* [2006], calculated using a direct integration method: both methods give similar results.

### 3.1. Density Profiles

[17] In region 1, the thermal electrons dominate the plasma density by two orders of magnitude. Their density maximizes near the planet and is observed to decrease with increasing radial distance. We however note that the spacecraft potential is negative in this region implying that we significantly underestimate the density of the thermal elec-

trons. Therefore, we use the total plasma densities derived from measurements of the upper hybrid frequency [*Persoon et al.*, 2005] by the Radio and Plasma Wave Science (RPWS) instrument [*Gurnett et al.*, 2004] in order to determine the true radial profile of the electron density ( $b = -3.9$ ). For this orbit, the RPWS densities were only available out to  $8 R_s$  because the upper hybrid resonance emission band becomes weak and sporadic beyond  $8 R_s$  [*Persoon et al.*, 2005]. The density of the suprathermal electrons is observed to increase sharply with increasing radial distance ( $b = 5.1$ ), peaking around  $9 R_s$ . In region 2, the densities of both the thermal and suprathermal electrons are observed to decrease with increasing radial distance.



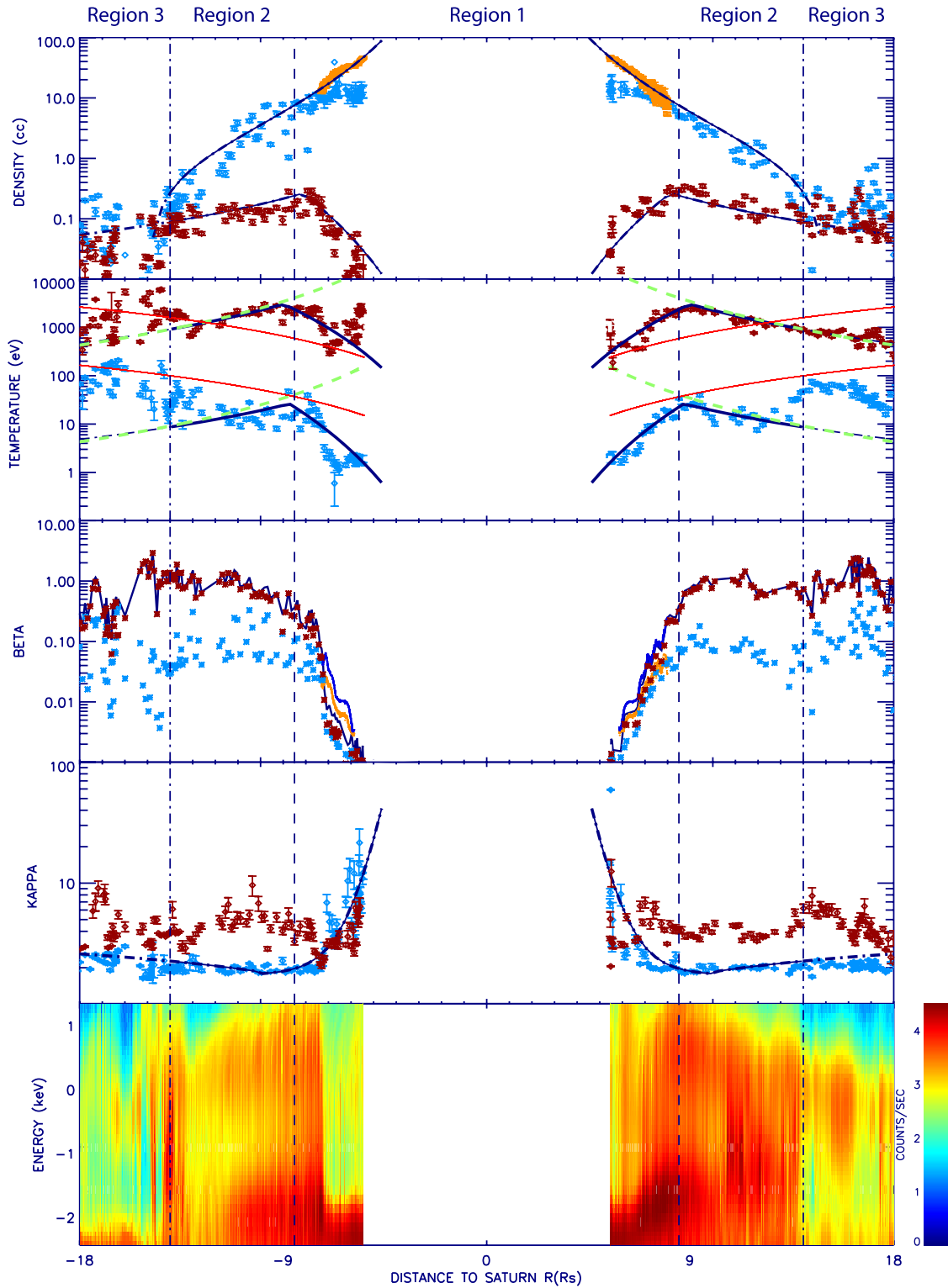


**Figure 3.** From top to bottom are shown thermal (in blue) and suprathermal (in red) electron densities, electron temperatures, electron beta, kappa indices, and color-coded CAPS/ELS energy-time spectrogram, versus radial distance). The total electron density deduced from the Upper Hybrid Frequency (UHF) technique [Persoon *et al.*, 2005] is indicated in orange. The overplotted black lines are the power law models adjusted to density, temperature and kappa profiles in regions 1 and 2. In the second panel, the proton and water-group ions corotational energy are shown in light red color, and profiles of constant first adiabatic invariant (thermal: 0.125 MeV/Gauss, suprathermal: 12.5 MeV/Gauss) are plotted in green dashed lines. The time resolution is 20 min. Vertical lines delineate the various boundaries identified and discussed in the text. The local time coverage goes from 0500 (night/dawn sector) to 2100 (night/dusk sector).

**Table 1.** Values of Parameters  $a$ ,  $b$ , and  $c$  in the  $aL^{b+c}$  Model for Regions 1 and 2

	$a$	$b$	$c$
<i>Region 1</i>			
$N_{\text{ecold}} (\text{cm}^{-3})$	$3.8 \times 10^4$	$-3.9$	$-$
$T_{\text{ecold}} (\text{eV})$	$6.8 \times 10^{-5}$	$5.9$	$-$
$N_{\text{ehot}} (\text{cm}^{-3})$	$4.8 \times 10^{-6}$	$5.1$	$-$
$T_{\text{ehot}} (\text{eV})$	$0.2$	$4.3$	$-$
$\kappa_{\text{cold}}$	$2.4 \times 10^9$	$-11.4$	$1.9$
$\kappa_{\text{hot}}$	$-$	$-$	$-$
<i>Region 2</i>			
$N_{\text{ecold}} (\text{cm}^{-3})$	$3.9 \times 10^4$	$-3.9$	$-0.9$
$T_{\text{ecold}} (\text{eV})$	$4245$	$-2.3$	$-$
$N_{\text{ehot}} (\text{cm}^{-3})$	$13.9$	$-1.9$	$-$
$T_{\text{ehot}} (\text{eV})$	$1.2 \times 10^6$	$-2.7$	$-$
$\kappa_{\text{cold}}$	$0.2$	$0.6$	$1$
$\kappa_{\text{hot}}$	$-$	$-$	$-$

The density gradient of the former population ( $b = -3.9$ ) is sharper than the gradient of the latter population ( $b = -1.9$ ). In the case of the thermal electrons, our results suggest that the RPWS profile obtained inside  $8.3 R_s$  could possibly be extrapolated to larger distances. In region 3, the densities of both thermal and suprathermal populations appear to be of the same order and very variable.

### 3.2. Temperature Profiles

[18] In region 1, the thermal electron temperature increases from 2 to 30 eV ( $b = 5.9$ ). The suprathermal electron temperature is also observed to increase with increasing radial distance, from 100 eV at closest approach to a maximum of 2 keV ( $b = 4.3$ ) at  $9 R_s$ . In region 2, cold and hot temperatures decrease with increasing radial distance with similar index  $b = -2.3$  and  $b = -2.7$ , respectively. In region 3, in parallel to its density profile, the thermal electron temperature profile becomes more variable, reaching a maximum around  $15 R_s$ . There is no obvious change in the hot electron profile trend between regions 2 and 3, mostly in the outbound leg. Indeed, the parameters of the model derived for the temperature profiles observed in region 2 are also valid in region 3.

### 3.3. Electron Beta Profiles

[19] In region 1, the thermal component dominates the overall pressure (yellow and light red curves in the third panel of Figure 3) and electron beta evolves from a few 0.001 to 0.1 at the outer boundary. The contribution of the suprathermal population increases quickly with increasing radial distance in region 1, until dominating the total pressure in region 2 where the electron beta reaches its maximum with a value close to 1. Farther out, the electron beta profile becomes smoother and undergoes smaller variations. This profile is comparable to the one determined at the magnetic equator by Maurice *et al.* [1996] (see their Figure 9) from Voyager 1 results. We also find that the electron beta is quite close to the ion beta profile calculated by Sergis *et al.* [2007] for equatorial orbits.

### 3.4. Kappa Profiles

[20] In region 1, the kappa index of thermal electrons drop off sharply, from very high values ( $\simeq 100$ ) at  $5.4 R_s$  to very low values ( $\simeq 2$ ) at the outer edge of the region ( $b =$

$-11$ ). The kappa index of the suprathermal electrons is however too variable to infer some conclusions about a specific trend. In region 2, kappa values of cold electrons tend to increase very slowly. Again, no hot kappa index profile trend is obvious in the observed data, with average values around 4. In region 3, the kappa index remains more or less constant (values between 2 and 3) for the two populations. Mauk *et al.* [2005] reported a lot of injection events in the inner magnetosphere which could be the origin of the observed variability in the kappa index of the hot electrons.

### 3.5. Pitch Angle Distribution

[21] We now consider the radial distribution of electron pitch angles in order to complete our description. Figure 4 displays the corresponding pitch angle-radial distance spectrogram at selected electron energies in the CAPS/ELS range. From this radial profile, we can identify one striking plasma boundary at  $7 R_s$ . In region 1, electrons are trapped and have pancake or butterfly pitch angle distributions at all energies as first revealed by Burch *et al.* [2007]. In region 2, electrons have bidirectional pitch angle distributions at all energies. The evolution from butterfly to bidirectional distributions appears to be function of electron energy, being smoother with increasing electron energy. In region 3, we again observe much more variability, with a quasi-periodic alternance of pancake and field-aligned distributions at about the planetary spin period.

[22] The isotropy hypothesis we thus used to calculate the moments (cf. section 2) is therefore valid for region 1, but not always for the outer regions, and the total moments we calculate there could be slightly modified once we will take into consideration the observed anisotropy in a future study.

## 4. Discussion and Conclusion

[23] On the basis of an electron isotropy assumption, we constructed a two-kappa model for the observed bimodal electron population according to the observed distribution function out-of-equilibrium state. This is in agreement with inferences by Collier [2004], who argues that in magnetospheric environments kappa distributions are more probable than maxwellian ones because of the occurrence of dynamic events implying changes in total average energy. In the whole radial range, the kappa index of the suprathermal population appears to be low whereas the thermal population is close to maxwellian near the planet (high densities) and evolves towards a more kappa-like distribution outwards (Figure 3).

[24] In the scenario proposed by Rymer *et al.* [2007], the thermal electron component is supposed to be produced in the inner magnetosphere by ionization of neutrals in Saturn's neutral cloud, while suprathermal electrons originating from the middle or outer magnetosphere diffuse into the inner magnetosphere via flux tube interchange with outward drifting cold plasma. We test this circulation pattern using electron moments and pitch angle analysis.

[25] Suprathermal electrons transported from the outer magnetosphere (region 3) are characterized by field-aligned pitch angle distributions in the region beyond  $9 R_s$ . These bidirectional distributions suggest first the ionosphere as the most probable source of these populations observed and

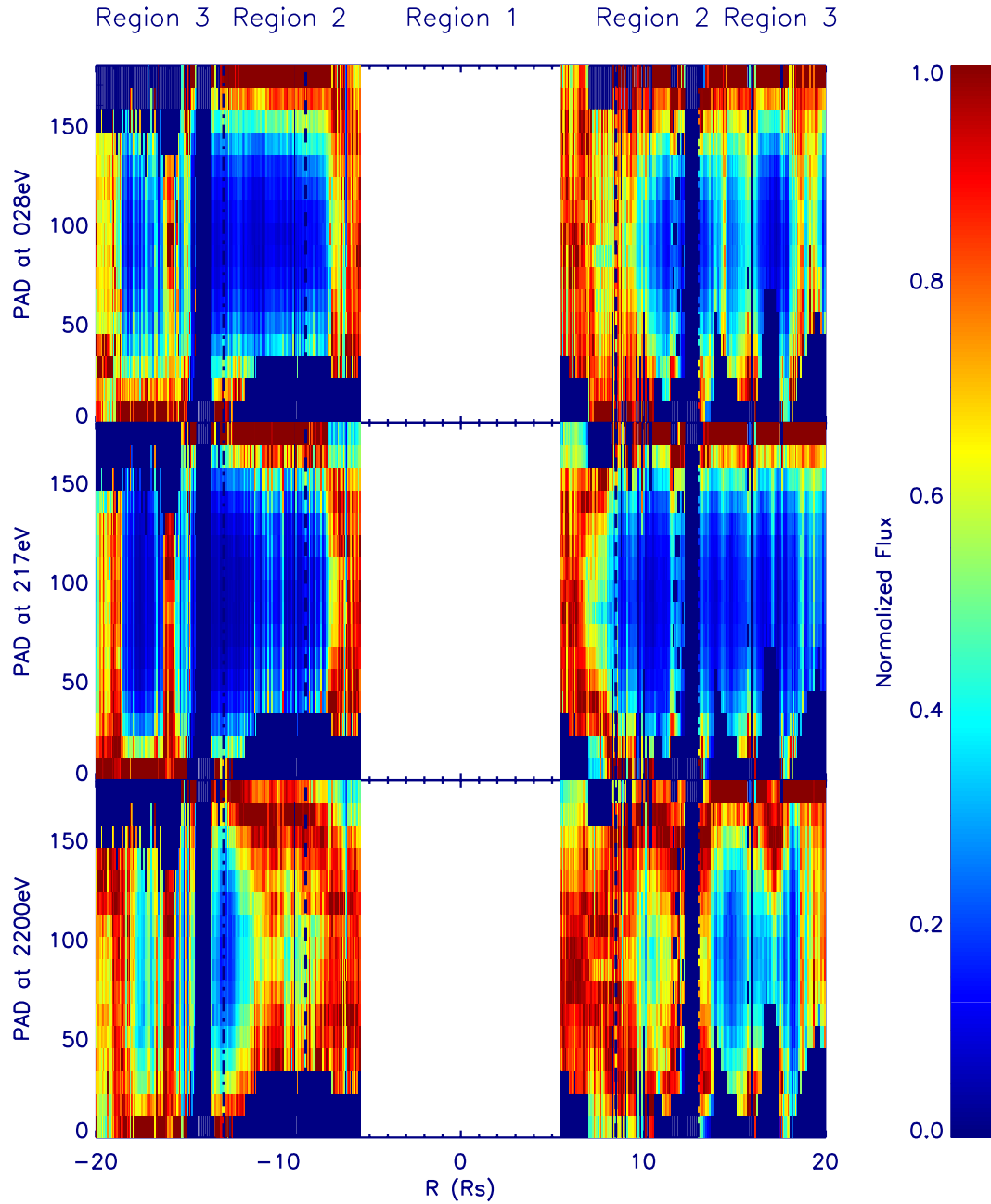


**Figure 4.** Color-coded CAPS/ELS pitch angle (in degrees) distribution versus radial distance, at selected electron energies (28, 217, and 2200 eV). The time resolution is 10 min. The dashed vertical lines separate the various regions identified and discussed in the text.

second, loss or scattering processes acting on  $90^\circ$  pitch angle electrons. As hot electrons are transported planetward in a more dipolar magnetic field configuration, they gain some perpendicular energy such that temperatures are observed to follow the  $\mu = 12.5 \text{ MeV/Gauss}$  adiabatic invariant energy profile (Figure 3) resulting in a more pancake-like distribution (Figure 4). At about  $9 R_s$ , the electrons penetrate into a region of higher neutral density. Sudden cooling and disappearance of high-energy electrons inside  $9 R_s$  may be explained by enhanced electron impact ionization of the neutral cloud as suggested by Santos-Costa *et al.* [2007]. In their scheme, energy from the incident impacting electron is partitioned into the two emerging

electrons: one low-energy electron (a few eV) diffusing with a random pitch angle and one high-energy electron diffusing with some preferential pitch angle direction and which is able to ionize in turn another neutral, cascading to lower energies via multiple collisions. The electron impact mechanism also seems to explain the observed thermal electron moment profiles in region 1: temperature lies in the range predicted by this model (a few eV), decreases inward as a consequence of colder electron impacts, and density enhances as neutral cloud density increases closer to the planet. The electron-neutral impact cross section on  $\text{H}_2\text{O}$  and  $\text{O}_2$  molecules is negligible for the thermal ( $\approx 10$  eV) electrons (unable to ionize in turn the neutral cloud), high at

intermediate energies (100 eV to 4 keV) and decreases in the higher-energy range (beyond 5 keV). We however observe depletion in the highest-energy electron intensities, which means these likely undergo other sinks mechanisms as absorption by satellite surface and collisions with E-ring dust particles in the inner magnetosphere [Roussos *et al.*, 2007].

[26] The thermal electron component is therefore produced in region 1 from the inner source associated with the neutral cloud, and starts with an isotropic distribution (Figure 5). In region 2, it experiences outward transport, consistent with temperature decrease following the  $\mu = 0.125 \text{ MeV/Gauss}$  adiabatic invariant energy profile (Figure 3) and pitch angle evolution from isotropic towards field-aligned distributions.

[27] The narrow boundary region close to  $9 R_s$  between regions 1 and 2 is ubiquitous and is seen in plasma moment profiles where a turnover is observed, and pitch angle distributions where they evolve fast from pancake to field-aligned distributions at all energies. A similar pitch angle evolution has been reported by Tomás *et al.* [2004a, 2004b] in the Jovian magnetosphere. Outward (inward) adiabatic transport can generate field-aligned (pancake) distributions. This process is discussed in more detail in the electron recirculation models proposed by Nishida [1976] and more recently by Rymer *et al.* [2008]. Interestingly, antiplanetward beams of electrons in the MIMI/LEMMS energy range have been reported by Saur *et al.* [2006] during early Cassini orbits. These beams were observed beyond  $11 R_s$ , along field lines that map into the auroral regions of Saturn. In addition, observational evidence for enhanced wave activity and pitch angle scattering of electrons by equatorial whistler mode emissions have been reported in the E-ring during the Voyager flybys by Scarf *et al.* [1983].

[28] The present paper describes a first step at unifying CAPS/ELS and MIMI/LEMMS electron observations in the Saturnian magnetosphere. We adjust a two-kappa model to the resulting composite spectra in order to calculate a set of three parameters (density, temperature, kappa index) for the observed thermal and suprathermal electron populations. We use these parameters together with electron pitch angle to detail the large-scale structure of the Saturnian electron populations based on a single pass, identifying relevant plasma boundaries and processes. We propose a unifying scenario for radial transport and mutual interactions of the two electron populations. Future work will include an extension of our analysis to other equatorial and nonequatorial orbits, in order to generalize our conclusions and to look for local time and longitude asymmetries in electron parameters.

## Appendix A: Methodology

### A1. Data Reduction and Background Subtraction

#### A1.1. CAPS/ELS

[29] The ELS data are corrected for the positive spacecraft potential outside  $7 R_s$  following the method detailed by Lewis *et al.* [2008]. We evaluated the negative spacecraft potential using the RPWS densities and our (under)estimated thermal densities. We checked that temperatures were hardly affected by this potential effect.

[30] The penetrating radiation value is defined as the minimum count in the high-energy channels of the ELS

detector (from 100 eV to 7 keV). The signal noise is defined as the root mean square value of the radiation value. These values are then subtracted from each energy bins of the ELS detector. We tested our method by comparing the radiation-corrected electron energy spectra measured outside a satellite absorption signature with the energy spectra measured inside the signature, where no penetrating particles are supposed to be (E. Roussos, private communication, 2007). This results in very similar spectra and validates our method, at least at first order.

[31] The obscuration problem is avoided by using mainly the anode 5 (in consistency with our assumption of isotropy) which is not affected by the RTG shield, the LEMMS instrument or the High-Gain Antenna (cf. Figure 5 of Young *et al.* [2005]).

#### A1.2. MIMI/LEMMS

[32] High-resolution data were averaged over one nominal period of 86 s, corresponding to one MIMI/LEMMS rotation when it was still rotating. These were then filtered using a quartile filtering (J. Manweiler, private communication, 2006), which allows to remove the possible light contamination.

[33] Penetrating particles from radiation belts contaminate the LEMMS low-energy channels above 100 keV [Roussos *et al.*, 2007]. There is no correction to this issue but the concerned channels were not taken into account in the flux spectra adjustment process. There is no obscuration problem since the LEMMS instrument is fixed to a right and safe position.

### A2. Geometric Factors

[34] The CAPS/ELS energy passbands and geometric factor considered in the present study are detailed by Lewis *et al.* [2008, cf. Table 1 and Figure 4]. The MIMI/LEMMS energy passbands and geometric factor passbands of the C0-C7 channels considered in the present study are defined in Table XIV of Krimigis *et al.* [2004].

### A3. Interpolation Between the Upper ELS and Lower LEMMS Energy Limits

[35] Depending on the considered region, the gap between the ELS and LEMMS fluxes in the energy range where both instruments overlap is more or less important. The main origin of this problem is the low ELS count rate at high energies, which is close to the background noise. In general, we only consider the ELS energy channels below 15 keV and simply interpolate linearly between the last value in this energy range and the first value in the LEMMS energy range.

### A4. Bimodal Models

[36] Three bimodal models were used to tentatively fit the electron Differential Number Flux DNF composite spectra. The Maxwellian and Kappa [Vasyliunas, 1968] distribution functions used in these models are given by the following expressions

$$f_{\text{Maxwell}}(v) = n \left( \frac{m}{2\pi k_B T} \right)^{3/2} \exp(-mv^2/k_B T) \quad (\text{A1})$$

$$f_{\text{Kappa}}(v) = \frac{n\Gamma(\kappa + 1)}{\omega_0^3 \pi^{3/2} \kappa^{3/2} \Gamma(\kappa - 1/2)} \left[ 1 + \frac{v^2}{\kappa \omega_0^2} \right]^{-\kappa-1} \quad (\text{A2})$$



We then compute the  $DNF$  from the distribution function  $f(v)$  using the relation

$$DNF = f(v) * \frac{v^2}{m} \quad (A3)$$

The contributions from both the thermal and suprathermal electron populations are summed to obtain the total  $DNF$

$$DNF_{total} = DNF_{thermal} + DNF_{suprathermal} \quad (A4)$$

Depending on the bimodal model considered, there are four (2-Maxwellian model), five (1-Maxwellian + 1-Kappa model), or six (2-Kappa model) free parameters. The adjustment process requires some initialization of these parameters. The densities are initialized at  $1 \text{ cm}^{-3}$  and the temperatures with values close to the energy of the peaks observed in the spectra. The kappa index of the thermal electron population is initially set to a high value and the kappa index of the suprathermal electron population to approximate the slope of the tail of the  $DNF$ . We then apply a Levenberg-Marquardt least squares method to obtain the optimal parameters that fit at best the composite  $DNF$  spectra. We actually fit the logarithm of the data because the dynamic flux range is very large.

## Appendix B: Isotropy Assumption

[37] We made the isotropy assumption to compute electron moments as electrons are supposed to exchange energy rapidly. This assumption is valid inside  $7 R_s$ . However, outside this region both cold and hot electrons seem to have field-aligned distributions. During the pass, particle measurement display a large pitch angle field of view thanks to the actuators and spacecraft rotation. Averaging the flux measurements on interval times covering sufficient wide pitch angle ranges (both perpendicular and parallel to the magnetic field) will give an isotropic equivalent flux number of the original anisotropic flux. In a following study, we will take into account the observed anisotropy and estimate the resulting perpendicular and parallel temperatures.

[38] **Acknowledgments.** We would like to acknowledge the two referees for their useful comments and suggestions.

[39] Wolfgang Baumjohann thanks Nick Sergis and Elias Roussos for their assistance in evaluating this paper.

## References

- Bridge, H. S., et al. (1981), Plasma observations near Saturn-Initial results from Voyager 1, *Science*, *212*, 217–224.
- Bridge, H. S., et al. (1982), Plasma observations near Saturn-Initial results from Voyager 2, *Science*, *215*, 563–570.
- Burch, J. L., J. Goldstein, W. S. Lewis, D. T. Young, A. J. Coates, M. K. Dougherty, and N. André (2007), Tethys and Dione as sources of outward-flowing plasma in Saturn's magnetosphere, *Nature*, *447*, 833–835, doi:10.1038/nature05906.
- Collier, M. R. (2004), Are magnetospheric suprathermal particle distributions ( $\kappa$  functions) inconsistent with maximum entropy considerations?, *Adv. Space Res.*, *33*, 2108–2112, doi:10.1016/j.asr.2003.05.039.
- Frank, L. A., et al. (1980), Plasmas in Saturn's magnetosphere, *J. Geophys. Res.*, *85*, 5695–5708.
- Gurnett, D. A., et al. (2004), The Cassini Radio and Plasma Wave Investigation, *Space Sci. Rev.*, *114*, doi:10.1007/s11214-004-1434-0.
- Krimigis, S. M., T. P. Armstrong, W. I. Axford, C. O. Bostrom, G. Gloeckler, E. P. Keath, L. J. Lanzerotti, J. F. Carbary, D. C. Hamilton, and E. C. Roelof (1981), Low-energy charged particles in Saturn's magnetosphere - Results from Voyager 1, *Science*, *212*, 225–231.
- Krimigis, S. M., J. F. Carbary, E. P. Keath, T. P. Armstrong, L. J. Lanzerotti, and G. Gloeckler (1983), General characteristics of hot plasma and energetic particles in the Saturnian magnetosphere - Results from the Voyager spacecraft, *J. Geophys. Res.*, *88*, 8871–8892.
- Krimigis, S. M., et al. (2004), Magnetosphere Imaging Instrument (MIMI) on the Cassini Mission to Saturn/Titan, *Space Sci. Rev.*, *114*, 233–329, doi:10.1007/s11214-004-1410-8.
- Lewis, G. R., et al. (2008), Derivation of density and temperature from the Cassini-Huygens CAPS Electrons Spectrometer, *Planet. Space Sci.*, *56*, 901–912, doi:10.1016/j.pss.2007.12.017.
- Mauk, B. H., et al. (2005), Energetic particle injections in Saturn's magnetosphere, *Geophys. Res. Lett.*, *32*, L14S05, doi:10.1029/2005GL022485.
- Maurice, S., E. C. Sittler, J. F. Cooper, B. H. Mauk, M. Blanc, and R. S. Selenick (1996), Comprehensive analysis of electron observations at Saturn: Voyager 1 and 2, *J. Geophys. Res.*, *101*, 15,211–15,232, doi:10.1029/96JA00765.
- Nishida, A. (1976), Outward diffusion of energetic particles from the Jovian radiation belt, *J. Geophys. Res.*, *81*, 1771.
- Persoon, A. M., D. A. Gurnett, W. S. Kurth, G. B. Hospodarsky, J. B. Groene, P. Canu, and M. K. Dougherty (2005), Equatorial electron density measurements in Saturn's inner magnetosphere, *Geophys. Res. Lett.*, *32*, L23105, doi:10.1029/2005GL024294.
- Randall, B. A. (1994), Energetic electrons in the magnetosphere of Saturn, *J. Geophys. Res.*, *99*, 8771.
- Roussos, E., G. H. Jones, N. Krupp, C. Parancas, D. G. Mitchell, A. Lagg, J. Woch, U. Motschmann, S. M. Krimigis, and M. K. Dougherty (2007), Electron microdiffusion in the Saturnian radiation belts: Cassini MIMI/LEMMS observations of energetic electron absorption by the icy moons, *J. Geophys. Res.*, *112*, A06214, doi:10.1029/2006JA012027.
- Rymer, A. M., et al. (2007), Electron sources in Saturn's magnetosphere, *J. Geophys. Res.*, *112*, A02201, doi:10.1029/2006JA012017.
- Rymer, A. M., et al. (2008), Electron circulation in Saturn's magnetosphere, *J. Geophys. Res.*, *113*, A01201, doi:10.1029/2007JA012589.
- Santos-Costa, D., et al. (2007), Examining the dynamics of low-energy electrons in Saturn's magnetosphere by combining Cassini CAPS-ELS data with charged particle transport model, *Eos. Trans. AGU*, *88*(52), Fall Meet. Suppl., Abstract P43A-1027.
- Saur, J., et al. (2006), Anti-planeward auroral electron beams at Saturn, *Nature*, *439*, 699–702, doi:10.1038/nature04401.
- Scarf, F. L., D. A. Gurnett, W. S. Kurth, and R. L. Poynter (1983), Voyager plasma wave measurements at Saturn, *J. Geophys. Res.*, *88*(A11), 8971–8984.
- Sergis, N., et al. (2007), Ring current at Saturn: Energetic particle pressure in Saturn's equatorial magnetosphere measured with Cassini/MIMI, *Geophys. Res. Lett.*, *34*, L09102, doi:10.1029/2006GL029223.
- Sittler, E. C., Jr., K. W. Ogilvie, and J. D. Scudder (1983), Survey of low-energy plasma electrons in Saturn's magnetosphere: Voyagers 1 and 2, *J. Geophys. Res.*, *88*, 8847–8870.
- Sittler, E. C., Jr., et al. (2006), Cassini observations of Saturn's inner plasmasphere: Saturn orbit insertion results, *Planet. Space Sci.*, *54*, 1197–1210, doi:10.1016/j.pss.2006.05.038.
- Tomás, A., J. Woch, N. Krupp, A. Lagg, K.-H. Glassmeier, M. K. Dougherty, and P. G. Hanlon (2004a), Changes of the energetic particles characteristics in the inner part of the Jovian magnetosphere: a topological study, *Planet. Space Sci.*, *52*, 491–498, doi:10.1016/j.pss.2003.06.011.
- Tomás, A., J. Woch, N. Krupp, A. Lagg, K.-H. Glassmeier, and W. S. Kurth (2004b), Energetic electrons in the inner part of the Jovian magnetosphere and their relation to auroral emissions, *J. Geophys. Res.*, *109*, A06203, doi:10.1029/2004JA010405.
- Vasyliunas, V. (1968), A survey of low-energy electrons in the evening sector of the magnetosphere with OGO 1 and OGO 3, *J. Geophys. Res.*, *73*, 2839.
- Vogt, R. E., D. L. Chenette, A. C. Cummings, T. L. Garrard, E. C. Stone, A. W. Schardt, J. H. Trainor, N. Lal, and F. B. McDonald (1981), Energetic charged particles in Saturn's magnetosphere-Voyager 1 results, *Science*, *212*, 231–234.
- Vogt, R. E., et al. (1982), Energetic charged particles in Saturn's magnetosphere-Voyager 2 results, *Science*, *215*, 577–582.
- Young, D. T., et al. (2004), Cassini plasma Spectrometer Investigation, *Space Sci. Rev.*, *114*, 1–112, doi:10.1007/s11214-004-1406-4.
- Young, D. T., et al. (2005), Composition and dynamics of plasma in Saturn's magnetosphere, *Science*, *307*, 1262–1266, doi:10.1126/science.1106151.

N. André, Research and Scientific Support Department, European Space Agency, NL-2200 AG Noordwijk, Netherlands.

M. Blanc, I. Dandouras, and P. Schippers, Centre d'Etude Spatiale des Rayonnements, CNRS/Université Paul Sabatier, 9 avenue du Colonel Roche, Toulouse F-31028, France. (schipper@cesr.fr)

A. J. Coates, L. K. Gilbert, and G. R. Lewis, Mullard Space Science Laboratory, University College London, Dorking RH5 6NT, UK.

M. K. Dougherty, Department of Space and Atmospheric Physics, Imperial College London, London SW7 2BZ, UK.

D. A. Gurnett and A. M. Persoon, Department of Physics and Astronomy, University of Iowa, Iowa City, IA 52242-1479, USA.

S. M. Krimigis, Johns Hopkins University Applied Physics Laboratory, Laurel, MD 20723, USA.

N. Krupp, Max-Planck-Institut für Sonnensystemforschung, D-37191 Katlenburg-Lindau, Germany.

D. T. Young, Southwest Research Institute, 6220 Culebra Road, P. O. Drawer 28510, San Antonio, TX 78228-0510, USA.